NeuroImage 200 (2019) 250–258

Contents lists available at ScienceDirect

NeuroImage

journal homepage: www.elsevier.com/locate/neuroimage

Visualization of thalamic calcium influx with quantitative susceptibility mapping as a potential imaging biomarker for repeated mild traumatic brain injury

Ferdinand Schweser [a,b,*], Jenni Kyyriäinen [c], Marilena Preda [a,b], Asla Pitkänen [c], Kathryn Toffolo [d], Austin Poulsen [d], Kaitlynn Donahue [d], Benett Levy [d], David Poulsen [d]

[a] Buffalo Neuroimaging Analysis Center, Department of Neurology, Jacobs School of Medicine and Biomedical Sciences at the University at Buffalo, The State University of New York, Buffalo, NY, USA
[b] Center for Biomedical Imaging, Clinical and Translational Science Institute, University at Buffalo, The State University of New York, Buffalo, NY, USA
[c] Epilepsy Research Laboratory, A. I. Virtanen Institute for Molecular Sciences, University of Eastern Finland, PO Box 1627, FI, 70211, Kuopio, Finland
[d] Department of Neurosurgery, Jacobs School of Medicine and Biomedical Sciences at the University at Buffalo, The State University of New York, Buffalo, NY, USA

ARTICLE INFO

Keywords:
Repeated mild traumatic brain injury
Calcium
Quantitative susceptibility mapping
QSM
MRI
Biomarker
Fluid percussion injury
Rats

ABSTRACT

A key event in the pathophysiology of traumatic brain injury (TBI) is the influx of substantial amounts of Ca^{2+} into neurons, particularly in the thalamus. Detection of this calcium influx *in vivo* would provide a window into the biochemical mechanisms of TBI with potentially significant clinical implications. In the present work, our central hypothesis was that the Ca^{2+} influx could be imaged *in vivo* with the relatively recent MRI technique of quantitative susceptibility mapping (QSM). Wistar rats were divided into five groups: naive controls, sham-operated experimental controls, single mild TBI, repeated mild TBI, and single severe TBI. We employed the lateral fluid percussion injury (FPI) model, which replicates clinical TBI without skull fracture, performed 9.4 Tesla MRI with a 3D multi-echo gradient-echo sequence at weeks 1 and 4 post-injury, computed susceptibility maps using V-SHARP and the QUASAR-HEIDI technique, and performed histology. Sham, experimental controls animals, and injured animals did not demonstrate calcifications at 1 week after the injury. At week 4, calcifications were found in the ipsilateral thalamus of 25–50% of animals after a single TBI and 83% of animals after repeated mild TBI. The location and appearance of calcifications on stained sections was consistent with the appearance on the *in vivo* susceptibility maps (correlation of volumes: $r = 0.7$). Our findings suggest that persistent calcium deposits represent a primary pathology of repeated injury and that FPI-QSM has the potential to become a sensitive tool for studying pathophysiology related to mild TBI *in vivo*.

1. Introduction

Traumatic brain injury (TBI) accounts for up to 3.8 million emergency department visits in the U.S. each year (Kenzie et al., 2017). Approximately 80% of TBI-related visits to the emergency department are classified as mild (mTBI) based on the Glasgow Coma Scale (GCS). Increasing awareness of TBI and the potential long-term consequences of even mTBI may have contributed to the 47% increase in hospital visits for TBI between 2007 and 2013 (Center for Disease Control). Approximately 30% of patients who report to the emergency department with a mTBI go on to develop post concussive syndrome (PCS). The long-term consequences of single versus repeated mTBI remain to be determined (Fehily and Fitzgerald, 2017). However, exposure to repeated mTBI can exacerbate poor outcomes (Meconi et al., 2018). The challenge is to define diagnostic criteria that help identifying those patients at highest risk for developing PCS.

The standard of care for emergency evaluation of acute TBI is Computed Tomography (CT). However, neuroimagining findings are frequently normal following CT or conventional clinical magnetic resonance imaging (MRI) in the non-acute stage, currently preventing an assessment of long-term outcome (Wu et al., 2016). While recent advances in MRI techniques have revealed subtle tissue alterations on a group level, the limited statistical power of most studies leaves the translation to clinical practice on an individual patient level unachieved (Shah and Allen, 2017; Wu et al., 2016). Furthermore, the lack of an

* Corresponding author. Buffalo Neuroimaging Analysis Center, Department of Neurology, Jacobs School of Medicine and Biomedical Sciences at the University at Buffalo, The State University of New York, 875 Ellicott St, Buffalo, NY, 14203, USA.
E-mail address: schweser@buffalo.edu (F. Schweser).

https://doi.org/10.1016/j.neuroimage.2019.06.024
Received 25 February 2019; Received in revised form 3 June 2019; Accepted 11 June 2019
Available online 12 June 2019

Abbreviations

AAALACA	Association for Assessment and Accreditation of Laboratory Animal Care
CDC	Centers for Disease Control
CCI	controlled cortical impact
CT	computed tomography
FPI	fluid percussion injury
GCS	Glasgow Coma Scale
IACUC	Institutional Animal Care and Use Committee
MRI	magnetic resonance imaging
mIP	minimum intensity projection
MIP	maximum intensity projection
mTBI	mild traumatic brain injury
NBF	neutral buffered formalin
NSS	neurological severity score
PCS	post concussive syndrome
Ppb	parts per billion
QSM	quantitative susceptibility mapping
r-mTBI	repeated mild traumatic brain injury
s-mTBI	single mild traumatic brain injury
s-sTBI	single severe traumatic brain injury
TBI	traumatic brain injury

objective radiological biomarker for TBI-related injury represents a critical issue for the development and testing of pharmacological agents with the potential to improve neurological outcome following injury.

A key event in the pathophysiology of TBI is the dynamic molecular alteration of the N-methyl-D-aspartate receptor structure and function (Osteen et al., 2004), with the concomitant influx of substantial amounts of Ca^{2+} into the neurons, particularly in the thalamus (Osteen et al., 2001). Detection of the neuronal calcium influx and consequent calcium deposition *in vivo* would provide a window into the biochemical mechanisms of TBI with potentially significant clinical implications for the objective assessment of injury severity and drug development. The relatively recent technique of Quantitative Susceptibility Mapping (QSM) (Haacke et al., 2015; Liu et al., 2015; Reichenbach et al., 2015; Wang and Liu, 2015) can detect diamagnetic calcium phosphate deposits and distinguish them from paramagnetic iron (Chen et al., 2014; Ciraci et al., 2017; Deistung et al., 2013; Schweser et al., 2010; Straub et al., 2017) in microbleeds.

In the present work, our central hypothesis was that the Ca^{2+} influx in mTBI could be imaged *in vivo* with QSM.

2. Materials and methods

Fig. 1 summarizes the study design.

2.1. Animals

A total of 33 adult, male Wistar rats (Charles River Laboratories, Montreal, Canada) were divided into five groups: naive controls (no craniotomy, n = 3), sham-operated experimental controls (craniotomy without impact, n = 3), single mild TBI (s-mTBI, n = 12), repeated mild TBI (r-mTBI, n = 7), and single severe TBI (s-sTBI, n = 8).

Animals were single-housed in a temperature-controlled room (24 °C) maintained on a 12 h light/dark cycle. Food and water were available *ad libitum*. The animal facility was fully accredited by the Association for Assessment and Accreditation of Laboratory Animal Care (AAALAC) International. All procedures involving animals were performed according to the guidelines of Institutional Animal Care and Use Committee (IACUC).

2.2. Fluid percussion injury (FPI) model

We employed the curved-tip lateral fluid percussion injury (FPI) model (McIntosh et al., 1989; Rau et al., 2014, 2012), which replicates clinical TBI without skull fracture. Briefly, rats were anesthetized with 3% isoflurane to perform a 5 mm craniotomy over the right hemisphere, equidistant between the bregma and lambda and adjacent to the lateral ridge. Body temperature was maintained with a rectal probe and auto-feedback monitor set at 37 °C. We modeled s-mTBI by applying a single 1.5–1.7 atm pressure pulse to cause a 20 msec depression of the dura. Repeated pressure pulses once per week over four weeks modeled r-mTBI. Application of a single 2.8–3.0 atm pressure pulse modeled s-sTBI. We performed Neurological Severity Score (NSS) assessments to determine motor and sensory functional behavior at 24 h post-injury as previously described (Rau et al., 2014, 2012; Smith et al., 2018) to confirm the absence of functional impairment for controls, negligible functional impairment (NSS<6) for s-mTBI, and r-mTBI rats, and substantial impairment (NSS>10) for s-sTBI rats.

2.3. In vivo MRI

Rats in the s-mTBI (n = 7 of 12) and r-mTBI (all n = 6) groups were imaged at four weeks after the (first) injury (r-mTBI: one week after the final injury). Rats in the sham group, the experimental control group, and the s-sTBI group were imaged at five weeks after the surgery (controls at an equivalent age-matched time point).

We performed MRI with a 20 cm diameter horizontal-bore 9.4 Tesla magnet (Biospec 94/20 USR, Bruker Biospin) equipped with a gradient coil supporting 440 mT/m gradient strength and 3440 T/m/s maximum linear slew rate (BGA-12S HP; Bruker Biospin) using a multi-echo gradient echo sequence with 144 μm isotropic resolution (TE_1 = 2.31 ms, ΔTE = 3.10 ms, TR = 100 ms, 19° flip angle, 16 echoes, BW = 50 kHz, FOV = 30 × 30 × 14mm^3, matrix = 135 × 208 × 97). The scanner was operated with ParaVision (version 5.1; Bruker Biospin). We employed a cross-coil configuration with a four-channel receiver mouse-brain surface coil and a transmitter volume coil. We induced anesthesia

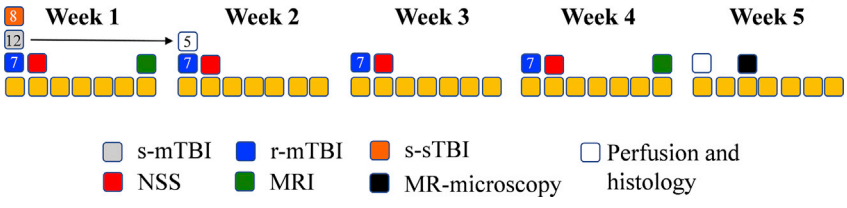

Fig. 1. Overall experimental design. Days are identified as yellow squares broken up into five periods of one week each. Single severe TBI (s-sTBI; orange squares), single mild TBI (s-mTBI; gray squares) and repeated mild TBI (r-mTBI; blue squares) are shown on the days of the respective injuries. Neurological severity scores (NSS; red squares) were recorded on the second day of each week following the respective injuries. MRI (green squares) was collected at the end of the first week and at the end of the fourth week, respectively. Post mortem MRIs (black squares) were conducted during week 5 following perfusion (white squares).

with 3–4% isoflurane in 1 L per minute of 100% medical-grade oxygen and maintained an anesthetic plane during MRI with 1–3% isoflurane. Rat respiration rate, pulse, arterial oxygen saturation, and body temperature were monitored continuously with an SpO_2-sensor attached to the animal's tail, a respiration pillow, and a rectal temperature probe (SA Instruments, Stony Brook, NY), respectively. The isoflurane concentration and the temperature of an integrated warm water bath in the animal bed (Thermo Fisher Scientific, Waltham, MA) were regulated to keep the respiration rate around 55–70 per minute and the core body temperature between 36.5 and 37 °C. We recorded the raw single-channel time-domain (k-space) data for offline QSM reconstruction.

We zero-padded the raw k-space to achieve a nominal isotropic spatial resolution of 96 μm. Susceptibility maps were reconstructed from these data with best-path phase unwrapping (Abdul-Rahman et al., 2007), multi-echo multi-channel phase combination (Robinson et al., 2011), R_2*-weighted field-mapping (Wu et al., 2012), V-SHARP (Özbay et al., 2017; Schweser et al., 2011; Wu et al., 2011), and QUASAR-HEIDI (Schweser and Zivadinov, 2018). For improved anatomical contrast on magnitude images, we averaged all magnitude images across different echo times. The averaging of the echoes substantially reduced respiration-related artifacts, which can be visible on individual echo images, and increased the contrast-to-noise ratio due to the high readout bandwidth (see above), while maintaining T_2*-weighted image contrast. All processing and reconstruction steps were performed fully automatically and reproducibly with in-house developed software in MATLAB (2013b, The MathWorks, Natick, MA) on a Ubuntu 12.04 high-performance computation server with 48 cores (Intel Xenon E5-2697v2 at 2.7Ghz) and 396 GB RAM.

2.4. MRI analysis

2.4.1. Image analysis

Three trained image analysts, blind to the study groups, assessed volume and susceptibility of thalamic calcifications, the volume of the lateral ventricles, and hemorrhage volumes in each rat using the 3D Slicer software platform. The ventricles were identified based on hyperintense contrast on the echo-averaged magnitude images, thalamic calcifications were identified as focal hypointense regions on magnetic susceptibility maps, and hemorrhages were identified as hypointense regions on the first echo magnitude images. Image contrast was adjusted individually for each modality to optimize visibility of ventricles and lesions, respectively. All identified regions were manually outlined on all slices on which they were present. Segmentations were refined by successively viewing all three slice orientations (coronal, horizontal, and sagittal). Calcifications and hemorrhages were only considered as "definite" if at least two of the three raters reported its presence. To minimize susceptibility blurring artifacts, we segmented hemorrhages based on corresponding focal hypointense regions on the magnitude images of the *first* echo (TE = 2.31 ms).

To improve the visibility of lesions in the publication figures, we calculated minimum intensity projections (mIPs) over 580 μm for the echo-averaged magnitude images. For susceptibility maps, we calculated both mIPs and maximum IPs (MIPs) to improve the visibility of calcifications and hemorrhages, respectively. We calculated the mIP and MIP images by selecting for each pixel the minimum and maximum intensity value across neighbouring slices, respectively.

2.4.2. Statistical analysis

We used paired (one-tailed) and two-sample (two-tailed) *t*-test, respectively, for comparisons between time points and groups. We used the free-marginal kappa to characterize the inter-rater agreement in the identification of thalamic calcification and Cohen's kappa to assess agreement between histology and MRI. Cohen's *d* was used to quantify effect sizes. We assessed the prevalence of calcifications using Fisher's Exact Test and used a significance threshold of $p = 0.05$ in all tests.

2.5. Histology and MR microscopy

2.5.1. Processing of tissue

Four weeks after the (first) injury, all rats except the controls were deeply anesthetized with isoflurane and perfused with 200 ml of saline for 10 min and 200 ml of 10% neutral buffered formalin (NBF) for 10 min at 1 week and 4 weeks after the TBI, respectively. The brains were removed from the skull, post-fixed in 10% NBF overnight at 4 °C, and placed into cryo-protectant solution [20% glycerol in 0.02M potassium phosphate buffered saline (pH 7.4)], and shipped to Finland for histologic processing. We perfused the n = 5 animals of the s-mTBI group that were not imaged at week 1 to study the appearance of calcium with histology shortly after the injury (vs. 4 weeks). We perfused one rat from the r-mTBI group that showed calcification on the *in vivo* scans with 10 mM gadobutrol (Gadavist, Bayer) and performed post-mortem MRI (Kim et al., 2009).

After arrival, the brains were frozen in dry ice and stored at −70 °C until further processed. Brains were sectioned in the coronal plane (1-in-12 series, 25 μm) with a sliding microtome (Leica SM, 2000, Leica Microsystems Nussloch GmbH, Nussloch, Germany). The first series of sections was stored in 10% formalin at room temperature and later stained with thionine (see below). The remaining series of sections were stored in tissue-collecting solution (30% ethylene glycol, 25% glycerol in 0.05 M sodium phosphate buffer, pH 7.4) at −20 °C until processed.

2.5.2. MR microscopy

Before shipping the tissue to Finland, we performed MR-microscopy of the animal perfused with gadobutrol at 36 μm isotropic spatial resolution (3D FLASH pulse sequence, TE = 4.14 ms, TR = 18.6 ms, averages = 8) with a dual-channel transmit-receive cryogenic surface coil (CryoProbe, Bruker Biospin). To improve the visibility of small hypointense structures (calcifications), we up-sampled the resolution to 24 μm isotropic via Fourier-based zero-filling, performed a non-parametric non-uniform B-spline-based intensity normalization [N4-ITK (Tustison et al., 2010) within the Advanced Normalization tools (ANTS) package v2.1 (Tustison et al., 2014)], and calculated mIPs over 480 μm for all three spatial directions separately.

2.5.3. Nissl staining

To assess the severity of neuronal damage after s-mTBI, r-mTBI or sTBI, the first series of sections were stained with thionine, cleared in xylene and cover-slipped using Depex® (BDH Chemical, Poole, UK) as a mounting medium.

2.5.4. Staining for calcifications

Every other section (600 μm apart) from an adjacent series of sections was stained with the Alizarin red-method (Makinen et al., 2008) to detect calcifications from the thalamus.

3. Results

3.1. Impact severity, mortality, apnea, and righting reflex

Injury severity was determined based on multiple parameters. The pressures used for inducing severe TBI (2.8–3.0 atm) resulted in average righting reflex times of 35 min and 45% mortality, resulting in n = 4 s-sTBI animals available for MRI. In contrast, the lower pressure range used for inducing mild TBI (1.5–1.7 atm) resulted in average righting reflex times of 5 min and no mortality. Typical apnea times of less than 2 min were observed after injury. One animal of the r-mTBI group had to be excluded from the study because it developed an infection, leaving a total of n = 6 animals in this group.

Fig. 2 shows the individual NSS trajectories for all animals. Sham-operated controls presented with an NSS between 0 and 1 at all time points (Fig. 2a), indicating no functional impairment. Animals with r-mTBI showed an average NSS of 3.2 ± 1.7 after the first injury, 2.2 ± 2.5

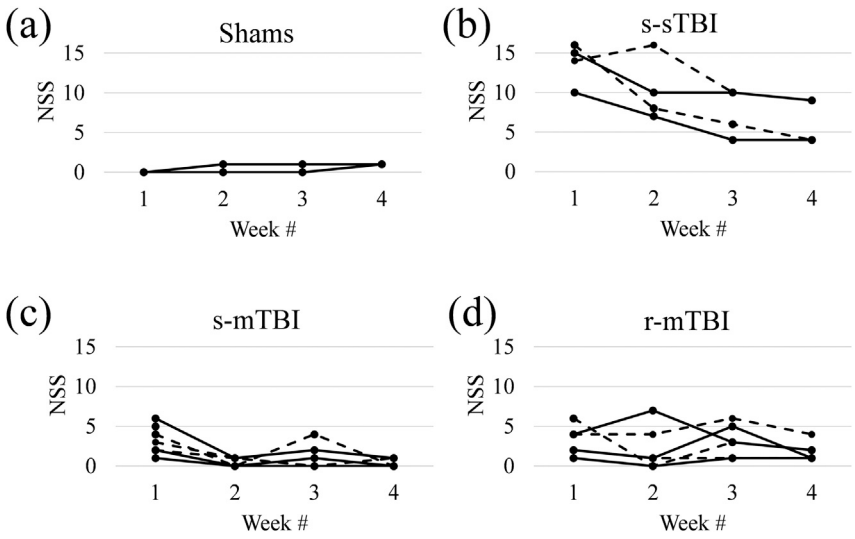

Fig. 2. Behavioral assessment with NSS at the different time points. Dashed and straight lines are used for improved visibility of individual trajectories. Panel (a) shows data of all three animals, but the data of two animals overlaps (line with lower NSS).

after the second, 3.2 ± 1.9 after the third, and 1.8 ± 1.1 after the fourth injury (Fig. 2d). Animals with an s-mTBI showed an NSS of 3.2 ± 1.5 after the first injury, similar to the r-mTBI group ($p = 1.0$), with a rapid recovery to the level of shams ($p > 0.3$) with 0.43 ± 0.49 at week 2, 1 ± 1.41 at week 3, and 0.29 ± 0.45 at week 4 (Fig. 2c). With 13.8 ± 2.3 at week 1, the s-sTBI animals demonstrated higher NSS compared to both mTBI groups ($p < 0.001$), which gradually recovered to 10.3 ± 3.5 at week 2 ($p < 0.006$), 7.5 ± 2.6 at week 3 ($p < 0.03$), and 6.5 ± 2.5 at week 4 ($p < 0.007$) (Fig. 2b).

3.2. MRI

All animals survived the imaging procedure. Due to technical issues with the imager, imaging failed in one animal of the s-mTBI group and one animal of the r-mTBI group at week 1. Of the 48 susceptibility maps, one map (s-mTBI at five weeks post-TBI) could not be analyzed due to artifacts. The final number of successful imaging experiments is summarized in Table 1.

3.2.1. Ventricular volume

Table 1 summarizes the measurements of ventricular volumes. In the sham group, volumes were comparable between shams and experimental controls ($p = 0.8$) and no interhemispheric differences were found in either group ($p \geq 0.25$). In all other groups, ipsilateral ventricles were enlarged compared to contralateral ventricles at 1 week and 4 weeks time-points ($p \geq 0.041$).

3.2.1.1. r-mTBI vs. s-mTBI:. At 1 week and 4 weeks time-points, the *contralateral* ventricular volumes were similar between the groups ($p > 0.37$). While, at week 4, the *ipsilateral* volumes were also similar between groups ($p = 0.52$), animals with r-mTBI showed 50% smaller ipsilateral volumes than rats with s-mTBI at week 1. However, this

Table 1
Summary of the results of the MR image analysis.

		Control	Sham	s-mTBI	r-mTBI	s-sTBI
Animals/group	week 1	3	3	6	5	–
	week 4	–	–	7 (6)[a]	6	4
Ventricles volume/mm^3	week 1	no MRI	no MRI	C: 6.8 ± 0.4 I: 12 ± 6 ($p = 0.036$)	C: 6.0 ± 1.2 I: 6.7 ± 1.3 ($p = 0.041$)	no MRI
	week 4	C: 7.78 ± 0.11 I: 8.0 ± 0.6 ($p = 0.35$)	C: 10 ± 3 I: 7.8 ± 0.9 ($p = 0.25$)	C: 10 ± 4 I: 17 ± 8 ($p = 0.025$)	C: 10 ± 3 I: 14 ± 6 ($p = 0.012$)	C: 20 ± 7 I: 34 ± 15 ($p = 0.022$)
	paired *t*-test	–	–	C: $p = 0.064$ I: $p = 0.049$	C: $p = 0.12$ I: $p = 0.030$	–
Hemorrhages, # of animals	week 1	no MRI	no MRI	C: 0 I: 6 (100%)	C: 0 I: 6 (100%)	–
	week 4	C: 0 I: 0	C: 0 I: 0	C: 0 I: 7 (100%)	C: 0 I: 6 (100%)	C: 0 I: 4 (100%)
Hemorrhages, volume/mm^3	week 1	no MRI	no MRI	–	–	no MRI
	week 4	–	–	1.0 ± 0.5	2.0 ± 0.8	0.94 ± 1.9
Calcifications, # of animals	week 1	no MRI	no MRI	0	0	no MRI
	week 4	0	0	3 (50%)	5 (83%)	1 (25%)
Calcifications, volume/mm^3	week 1	no MRI	no MRI	–	–	–
	week 4	–	–	0.04 ± 0.04	0.3 ± 0.3	0.12 ± 0.00
	paired *t*-test	–	–	$p = 0.13$	$p = 0.041$	–
Calcifications, susceptibility/ppb	week 1	no MRI	no MRI	–	–	–
	week 4	–	–	-56 ± 30	-56 ± 19	-60.4 ± 0.0

Values are reported as mean ± standard deviation. "I" and "C" denote ipsilateral (right) and contralateral (left) hemisphere, respectively. "# of animals" is the number of animals in which hemorrhage/calcification was observed. Group averages of calcification volume were calculated using only animals in which calcification was found, which implies that the stated values represent the average volume of identified lesions. The paired *t*-test used a volume of 0 mm^3 if no lesion was found at week 1.

[a] The susceptibility map of one of the s-mTBI animals at week five could not be analyzed due to motion artifacts.

difference did not reach statistical significance ($p = 0.10$). The higher average volume in s-mTBI was driven by two animals with particularly large ventricles (16.3 mm^3 and 23.3 mm^3, respectively). Exclusion of these animals rendered the volume in the s-mTBI more similar to that in the r-mTBI group (s-mTBI $8.3 \pm 1.9\,mm^3$ vs. r-mTBI $6.7 \pm 1.3\,mm^3$ at week 1; s-mTBI $13 \pm 7\,mm^3$ vs. r-mTBI $14 \pm 6\,mm^3$ at week 2; $p \geq 0.27$). We have occasionally observed enlarged ventricles in control animals of the strain used (Wistar), suggesting that the particularly large ventricles in these animals may not be necessarily related to the injury model. Ventricular volumes were higher in both groups and both hemispheres at week 4 compared to week 1, but the differences reached statistical significance only in the ipsilateral hemisphere (paired *t*-test, $p < 0.049$).

3.2.1.2. s-sTBI vs. s-mTBI:. Animals with s-sTBI showed, on average, 100% larger ventricles compared to s-mTBI animals, but the difference did not reach statistical significance ($p > 0.12$), probably due to the relatively small number of animals per group.

3.2.2. Hemorrhages

In line with previous reports (Grossman and Inglese, 2015) QSM visualized FPI-induced hemorrhages at gray-white matter junctions (Fig. 3, MIPs) on the ipsilateral side but not at the contralateral side. Table 1 summarizes the quantitative results for hemorrhages. None of the sham or experimental control rats demonstrated intracerebral hemorrhages. At both weeks 1 and 4, we found definite hemorrhages in all injured rats (100%; s-s, s-m, and r-mTBI). At week 4, r-mTBI animals showed a significantly higher hemorrhage volume than s-mTBI ($2.0 \pm 0.8\,mm^3$ vs. $1.0 \pm 0.5\,mm^3$, $p = 0.037$) and s-sTBI groups ($0.94 \pm 0.19\,mm^3$, $p = 0.0075$). Hemorrhagic volumes were similar between s-mTBI and s-sTBI groups ($p = 0.12$) at week 4. Determination of the volume of hemorrhages at week 1 was not successful. In five of the injured animals, hemorrhages were invisible on the first echo magnitude image at week 1 but appeared at week 4 (see Figure S1 in the Supplementary Materials). Since we observed this effect also in s-mTBI animals, we concluded that the observation was related likely to a change in magnetic susceptibility of blood during degradation, as reported previously (Chang et al., 2016), rendering a quantitative analysis of the hemorrhagic volume challenging. In particular, a comparison of determined volumes between week 1 and week 4 would be compromised by different susceptibility blooming artifact levels. We did not perform a statistical analysis of the average magnetic susceptibilities of identified hemorrhages because the lesions showed a substantial inhomogeneity on the susceptibility maps.

3.2.3. Thalamic calcification

Fig. 4a compares the appearance of thalamic calcification on different MRI contrasts. The magnitude-based contrasts (top row) showed signal alterations at the locations of calcium and blood deposits (red circles) but did not allow differentiating between the two types of lesions. The background-corrected phase image (bottom left) shows significant phase contrast in the region of the hemorrhage but diffuse contrast at the location of the calcification due to the non-local relationship between phase and the underlying magnetic susceptibility distribution (Schweser et al., 2016). The susceptibility map (bottom right) showed a clearly defined, focal calcification (hypointense) that could be unambiguously differentiated from hemorrhages (hyperintense).

Table 1 and Figs. 3 and 4 summarize the results of the analysis of thalamic calcifications. As expected, we did not find calcium deposits in the sham or experimental controls animals. We also did not find calcifications in any of the s-mTBI or r-mTBI scans at week 1. At week 4, calcifications were found in 50% (3/6) of s-mTBI animals, 83% (5/6) of r-mTBI animals, and 25% (1/4) of s-sTBI animals. Fig. 3 shows images of representative animals with identified thalamic calcification for each of the injury groups. The mIPs of the susceptibility maps indicated potential calcification also outside of the thalamus, particularly in the vicinity of the haemorrhages. We did not further confirm this observation as the study hypothesis was focused on thalamic calcification. Furthermore, in the direct vicinity to haemorrhages on susceptibility maps, the interpretation of hypointense signal is challenging as it may be related simply to incomplete inversion of the measured field (Sun et al., 2015).

Inter-rater agreement for the identification of calcifications was adequate ($\kappa > 0.7$) in experimental controls ($\kappa = 1.00$) and r-mTBI ($\kappa = 0.78$). A lower agreement was achieved in sham ($\kappa = 0.35$) and s-mTBI rats ($\kappa = 0.55$), and agreement equal to chance in s-sTBI ($\kappa = 0.00$).

The average magnetic susceptibility of identified definite calcifications was similar between groups ($p = 0.43$) with an average of -60 ± 20 parts-per-billion (ppb). Animals of the r-mTBI group showed the largest calcifications ($0.3 \pm 0.3\,mm^3$) and those of the s-mTBI group showed the smallest calcifications ($0.04 \pm 0.04\,mm^3$; see also Fig. 3 for a size-comparison). Despite a relatively high effect size of $d = 0.87$, the difference did not reach statistical significance ($p = 0.06$) likely because of the low number of calcifications in the s-mTBI group. Fig. 4c visualizes the

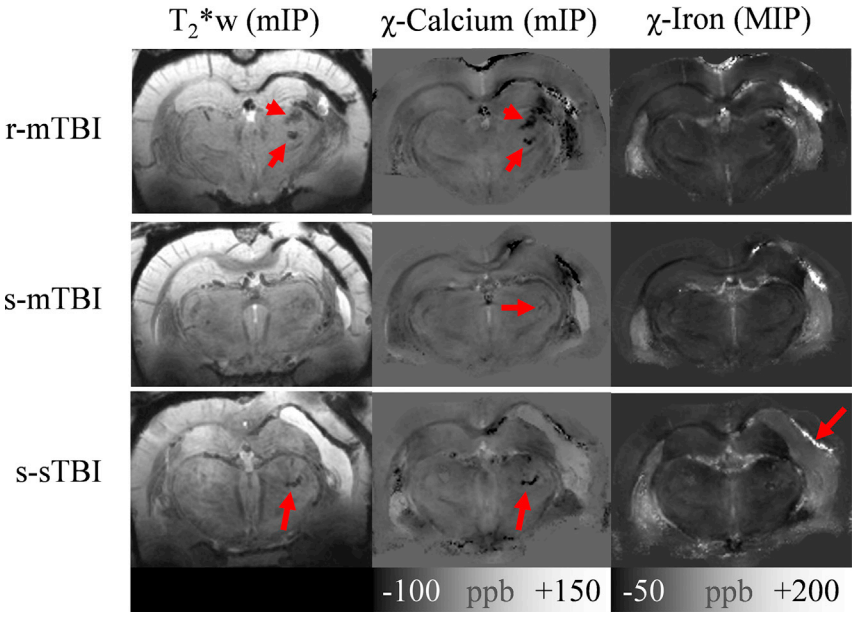

Fig. 3. Overview of *in vivo* imaging findings in the three injury groups. The top row shows the animal with r-mTBI that had the highest calcification volume (0.79 mm^3) at week 4. The middle row shows one of the three s-mTBI animals in which a calcification was identified at week 4 (0.0098 mm^3; confirmed by histology). The bottom row shows images of the only s-sTBI animal that showed a calcification on MRI (0.12 mm^3; confirmed by histology). Images in the left column are minimum intensity projections (mIPs) of the T_2*w magnitude images, those in the middle are mIPs of the susceptibility maps (delineating calcium deposits), and the images on the right show maximum intensity projects (MIPs) of susceptibility maps (delineating iron deposits). All projections were calculated over 580 μm.

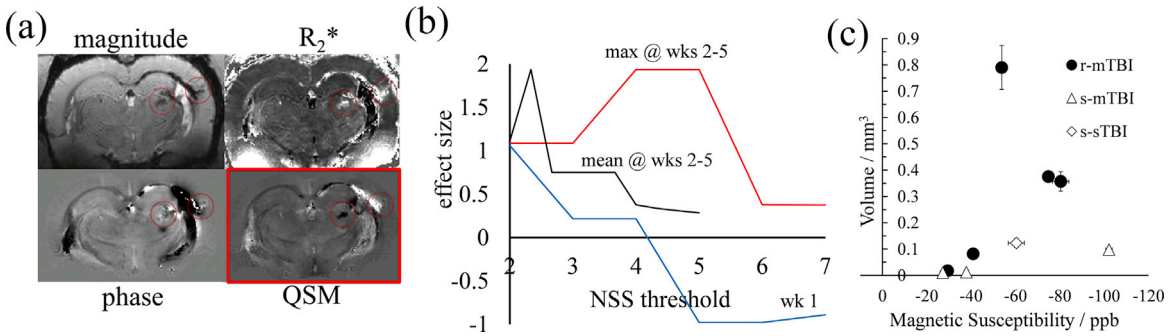

Fig. 4. Thalamic calcifications on MRI. (a) MR images of a representative r-mTBI animal. The top row shows the magnitude-based images: the echo-averaged magnitude image, and the R_2*-map (black to white: 0 … 100/s), respectively. The bottom row shows the phase-based images: the background-corrected phase image (the input to QSM) and the computed susceptibility map (−80 … +150 ppb), respectively. (b) The effect size of the difference in calcified volumes between two r-mTBI animal subgroups that were defined based on their NSS scores (abscissa). The blue line considered only the NSS at the first week for group splitting, the black line considered the average of NSS across weeks 2–4, and the red line considered only the maximum NSS of the animals across weeks 2–4. (c) Volume of thalamic calcifications over their magnetic susceptibility. Values of each animal were averaged across all three raters. Error bars indicate the standard deviation between raters.

volume of definite calcifications over their magnetic susceptibility for all animals studied, showing a high correlation between the quantities ($r = 0.92$).

The prevalence of calcifications was significantly higher in r-mTBI animals compared to shams and controls ($p = 0.015$) but not in s-mTBI or s-sTBI compared to shams and controls ($p > 0.4$). Differences in prevalence did not reach statistical significance when comparing individual injury groups with one another at week 4 ($p > 0.19$). Prevalence of calcification was significantly higher at week 4 compared to week 1 in r-mTBI ($p = 0.015$), but not in s-mTBI ($p = 0.45$).

We investigated the association between neurological disability and calcium deposition by splitting the r-mTBI group into a high- and a low-NSS group and assessing the difference in the group-average calcification volumes. First, we performed the splitting based on the maximum NSS score of each animal, representing the *maximum* neurological disability at any point in time. To study the effect of repeated injuries (second-hit hypothesis), we repeated the analysis excluding the first NSS score. Fig. 4b shows the effect sizes of the group differences in calcification volumes for both analyses. The maximum disability at the second or later hits predicted calcification volume with Cohen's effect size of $d = 1.94$ ($p = 0.037$) when groups were split at maximum NSS scores between 4 and 5. Average NSS across second and later injuries was a less robust predictor for calcification volume and NSS at the first time point did not exceed an absolute effect size of $d = |1.06|$.

Fig. 5 shows the MR microscopy of a r-mTBI animal with calcification along with corresponding sections of mIPs of the *in vivo* susceptibility maps (red boxes). The calcifications were granular in shape and located in both thalamic gray and adjacent white matter tracts. We observed a high agreement of geometrical features and location between *in vivo* susceptibility maps and postmortem MR microscopy. We observed in some cases that the hypointense calcification was surrounded by a bright rim (Fig. 6d, arrows), potentially related to iron-laden astrocytes (Meguro et al., 2008) as reported previously (Lehto et al., 2012).

3.3. Histology

Table 2 and Fig. 7 summarize the histological results.

3.3.1. Nissl

No neurodegeneration was observed in any of the sham-operated controls. However, TBI-related cortical damage was located laterally to the impact site covering mainly auditory and somatosensory cortex. The center of the cortical lesion was −3.80 mm posterior to bregma covering ±12 sections (total coverage 6900 µm). In s-mTBI, the lesion extended throughout layers 3–5 when in r-mTBI and s-sTBI cases the injury covered all the layers of the cortex. Typically, minimal cortical cell loss, white matter damage and gliosis was seen following s-mTBI. In one case, also thalamic damage was observed after s-mTBI. Contrary, clear tissue and cell loss was detected after r-mTBI and s-sTBI in the cortex and prominent gliosis and was seen in the cortex, thalamus, and hippocampus. Furthermore, white matter damage, mainly in the corpus callosum, was more prominent in r-mTBI and s-sTBI than in s-mTBI. Thalamic damage was the most obvious after r-mTBI. Furthermore, neurodegeneration such as hilar cell loss, thinning of the CA1 subfield and granule cell dispersion was also seen in different hippocampal subfields after r-mTBI and s-sTBI. In all cases, no clear damage was seen on the contralateral side.

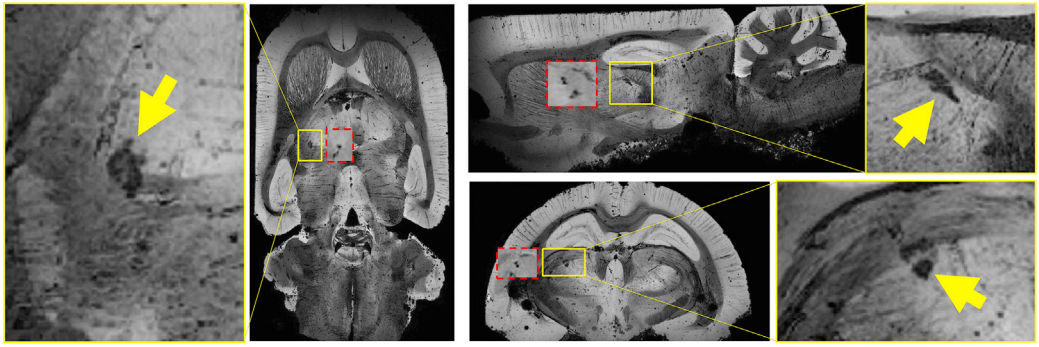

Fig. 5. Minimum intensity projections (mIPs) over 480 µm of MR-microscopy (MRM) images of an r-mTBI animal. The yellow inserts are magnifications of the MRM-mIPs showing the calcifications (arrows). The red inserts are mIPs over 1.16 mm of the *in vivo* susceptibility map of the same animal at a similar anatomical location.

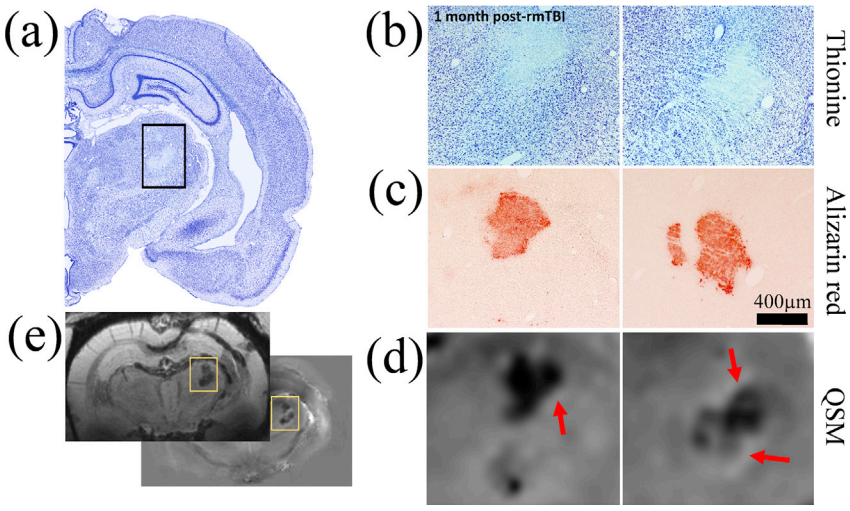

Fig. 6. Comparison of MRI-based findings with histology in an r-mTBI animal with 0.38 mm^3 thalamic calcification volume. **(a)** Low magnification picture of the thionine stained (neuronal damage) injured right hemisphere. **(b)** Higher magnification pictures of thionine stained the thalamus in two consecutive slides spaced 300 μm apart, showing thalamic damage. **(c)** Thalamic calcifications stained with Alizarin red (calcium). Note the similar location of the calcifications with thionine stained sections. **(d)** Magnifications of similar regions on the susceptibility maps with a nominal slice thickness of 90 μm. A high agreement of the appearance of calcium deposits was observed between MRI and histology. Red arrows point at the hyperintense rim observed around calcifications. **(e)** Overview slices of mean-intensity projections and mIPs of the susceptibility map and magnitude images, respectively, across the 600 μm covered by the shown histological stains.

Table 2
Histological results.

Time post-injury		Sham	s-mTBI		r-mTBI	s-sTBI
			1 week	4 weeks	4 weeks	4 weeks
Animals/group		3	5	**7**	**6**	4
Calcification, # of animals		0	0	3 (43%)	4 (67%)	2 (50%)
Histology+	# sections	0	0	2 ± 2	4 ± 2	2 ± 1
	MRI+	0	0	3 (50%)	4 (67%)	1 (25%)
	MRI-	0	0	0	0	1 (25%)
	MRI ±	0	0	3 (50%)	4 (67%)	2 (50%)
Histology-	MRI+	0	2 (40%)	0	1 (17%)	0
	MRI-	3 (100%)	3 (60%)	4 (67%)	1 (17%)	2 (100%)

Histology+ and Histology- indicate finding and absence of calcium deposits on Alizarin red sections, respectively. MRI+ and MRI- indicate finding and absence of calcium deposits on susceptibility maps, respectively. "# sections" lists average and standard deviation of the number of sections on which calcium was observed. Stated percentages indicated the fraction with respect to analyzable susceptibility maps (cf. Table 1) except for the total number of animals (# of animals) where it refers to all brains analyzed histologically.

3.3.2. Calcium

Histology did not report thalamic calcifications in shams or s-mTBI rats at 1-week post-TBI. However, histology reported thalamic calcification in 43% (3/7) of s-mTBI rats at 4 weeks post-TBI in 1, 2, and 4 consecutive slides, covering distances of 25 μm, 300 μm, and 1200 μm (1-in-12 series), respectively.

In the r-mTBI group, all except one calcification found on QSM were confirmed by histology. The volume of the missed calcification was 0.017 mm^3 on MRI, corresponding to an equivalent spherical radius of 160 μm (one voxel) and suggesting that histology missed the calcification identified on the susceptibility maps (see Fig. S2 in the Supplementary Materials).

Histology confirmed the calcification that was found with QSM in one of the s-sTBI rats. Also, histology revealed calcification in one section of another animal with s-sTBI (found on QSM by only one of the three raters), resulting in a total occurrence of thalamic calcification in 50% (2/4) of rats with s-sTBI. Considering all calcifications seen with histology or MRI (including cases with absence on either of both modalities) r-mTBI showed calcifications in 67% of the animals, followed by s-sTBI with 50%, and s-mTBI with 43% of the animals. Findings with histology and MRI are summarized for the different groups in Fig. 7a.

The location and appearance of calcifications on Alizarin red stained sections were highly similar to the appearance on the susceptibility maps (Fig. 6). Agreement between MRI and histology (Fig. 7b) was the highest in the s-mTBI group at 4 weeks (κ = 1. 0), followed by r-mTBI (κ = 0.57) and s-sTBI (κ = 0.5). The correlation coefficient between calcification volume on MRI and the number of histological sections in all animals

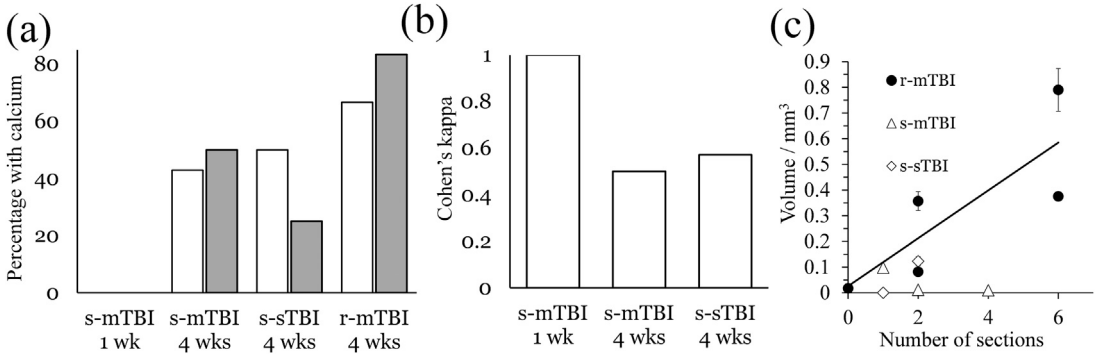

Fig. 7. Results of the histological analysis of calcium and comparison with MRI. (a) Percentage of animals with calcification identified on MRI (gray) and histology (white), respectively. (b) Agreement between MRI and histology for different groups. (c) Comparison of the size of calcifications on susceptibility maps (volume) and histology (number of sections). The correlation coefficient for all lesions was r = 0.70. The regression line describes the relationship for the r-mTBI group (0.093 mm^3 · n + 0.026 mm^3; n: number of sections).

with calcification was r = 0.70 (Fig. 7c).

4. Discussion

The present study is the first study that uses the ability of QSM to identify calcium deposits following TBI. Previous applications of QSM in a rodent model of TBI by Li et al. (2016) focused entirely on the investigation of the white matter. Another study by Liu et al. (2016) applied QSM in patients with TBI to quantify micro-bleed burden. The present study has confirmed that QSM can detect and quantify thalamic calcium influx associated with TBI reliably in rodents. Thalamic calcifications appeared as clearly delineated, focal hypointense lesions on susceptibility maps. The focal appearance of the lesions allows assessing this pathology-related marker on an individual-subject level and, if confirmed in humans, could represent an important step toward the clinical assessment of TBI-related pathology.

Only one of the MRI-detected calcifications could *not* be confirmed by histology. The small volume of the lesion on MRI suggests that histology, which analyzed 25 μm thick slices with a gap of 300 μm compared to the continuous 3D coverage with MRI, missed the lesion. Our results highlight the benefit of the employed tomographic imaging technique.

Using ^{45}Ca-autoradiography in brain specimens, Osteen et al. (2001) reported a delayed focal accumulation of Ca^{2+} in the thalamus beginning two to four days post-injury and progressing for up to two weeks. In the present work, we demonstrated that the recently developed advanced MRI technique of QSM can detect this clinically relevant pathology *in vivo*. The conventional MRI techniques to image susceptibility variations in biological tissues, T_2*-weighted imaging and phase contrast, were not able to differentiate between calcium and hemorrhages (Fig. 4a). Furthermore, the absence of calcifications in the s-mTBI group at week 1 and presence of calcifications in about 50% of the s-mTBI animals at week 4 confirmed the delayed nature of the calcium influx observed by Osteen and colleagues.

Using the controlled cortical impact (CCI) mouse model, Onyszchuk et al. (2009) found an accumulation of abnormal iron deposits, degenerating oligodendrocytes, and increased astrocyte and microglia staining in the ipsilateral thalamus at one and two months post-injury. At the same anatomical locations, the authors observed hypointensity on T_2-weighted MRI, which they interpreted as being causally related to the increased iron concentration. Our results using a more advanced MRI technique presented here suggest that the observed MRI hypointensity in that study was caused by calcium instead of iron accumulation. As Onyszchuk et al. discuss, heme-bound iron, which is generally not thought to be stained by the Perls procedure, may be released from degenerating thalamic neurons and be converted into free, more readily stainable iron. Previous research has shown that TBI causes elevated expression of heme oxygenase in the thalamus (Yi and Hazell, 2005). In the presence of imbalanced antioxidant defense, as it may be present after TBI, free iron is an essential catalyst of the Fenton chemistry, which results in hydroxyl radicals further promoting neuronal damage.

The amount of calcium deposited was the highest in the r-mTBI group, and substantially less calcium was observed in s-mTBI, suggesting that repeated injury is the primary driver of calcium deposition. Our observations also suggest an association between neurological disability and calcification volume (Fig. 4b). The observation that neurological disability after the second, third and fourth hits were more strongly associated with calcium deposition (Fig. 4b, red line) than the NSS at the first time point (Fig. 4b, blue line) suggests a link of thalamic calcification with the second impact syndrome.

The evidence is increasing for the involvement of thalamic damage in the pathophysiology of TBI and clinical impairment (Grossman and Inglese, 2015). The literature suggests that TBI exposes the thalamus to both primary and secondary injury (Grossman and Inglese, 2015) and future studies will have to elucidate to which of these mechanisms the observed calcium accumulation is related. The potential of monitoring thalamic tissue damage non-invasively via the appearance of calcification on MRI may represent an attractive means for the early prediction of long-term brain damage and cognitive outcome if thalamic calcification can be confirmed in the clinical setting and correlated with clinical deficits.

Limitations of our study primarily relate to the limited number of animals studied, which, combined with the inherent variability in the experimental procedure of the injury group, resulted in insufficient statistical power to elucidate associations between injury model type and calcification prevalence. Future studies should include more animals and perform imaging more often to better understand the temporal dynamics and dose dependency of tissue calcifications. Histological analyses may reveal if the appearance of MR-visible calcification precedes or follows neuronal damage. A long-term follow-up will reveal if the calcium deposits are transient or permanent.

5. Conclusion

The unique ability of QSM to differentiate between calcium phosphate (diamagnetic) and heme-iron (paramagnetic) unambiguously revealed thalamic calcium influx concomitant to mTBI. Hence, the technique has the potential to become a sensitive tool for studying mTBI pathophysiology and in drug development. In particular, our finding of significant concentrations of calcium in the r-mTBI model, but not in s-mTBI, suggests that persistent calcium deposits represent a primary pathology of repeated injury.

Funding

Research reported in this publication was funded by the National Center for Advancing Translational Sciences of the National Institutes of Health under Award Number UL1TR001412 (F.S.) and Academy of Finland Grants 272249 and 273909 (A.P.) The content is solely the responsibility of the authors and does not necessarily represent the official views of the NIH.

CRediT author statement

Ferdinand Schweser: Conceptualization, Methodology, Software, Validation, Formal Analysis, Resources, Data Curation, Writing – Original Draft, Writing – Review & Editing, Visualization, Supervision, Project Administration, Funding Acquisition. **Jenni Kyyriäinen:** Formal Analysis, Investigation, Data Curation, Writing – Review & Editing, Visualization. **Marilena Preda:** Investigation, Writing – Review & Editing. **Asla Pitkänen:** Conceptualization, Methodology, Resources, Writing – Review & Editing, Supervision, Funding Acquisition. **Kathryn Toffolo:** Investigation. **Austin Poulsen:** Data Curation, Investigation. **Kaitlynn Donahue:** Investigation. **Benett Levy:** Investigation. **David Poulsen:** Conceptualization, Methodology, Resources, Writing – Review & Editing, Supervision, Project Administration, Funding Acquisition.

Appendix A. Supplementary data

Supplementary data to this article can be found online at https://doi.org/10.1016/j.neuroimage.2019.06.024.

References

Abdul-Rahman, H.S., Gdeisat, M.A., Burton, D.R., Lalor, M.J., Lilley, F., Moore, C.J., 2007. Fast and robust three-dimensional best path phase unwrapping algorithm. Appl. Opt. 46, 6623–6635.

Chang, S., Zhang, J., Liu, T., Tsiouris, A.J., Shou, J., Nguyen, T.D., Leifer, D., Wang, Y., Kovanlikaya, I., 2016. Quantitative susceptibility mapping of intracerebral hemorrhages at various stages. J. Magn. Reson. Imaging 44, 420–425. https://doi.org/10.1002/jmri.25143.

Chen, W., Zhu, W., Kovanlikaya, I., Kovanlikaya, A., Liu, T., Wang, S., Salustri, C., Wang, Y., 2014. Intracranial calcifications and hemorrhages: characterization with quantitative susceptibility mapping. Radiology 270, 496–505. https://doi.org/10.1148/radiol.13122640.

Ciraci, S., Gumus, K., Doganay, S., Dundar, M.S., Kaya Ozcora, G.D., Gorkem, S.B., Per, H., Coskun, A., 2017. Diagnosis of intracranial calcification and hemorrhage in pediatric patients: comparison of quantitative susceptibility mapping and phase images of susceptibility-weighted imaging. Diagn Interv Imaging 4–11. https://doi.org/10.1016/j.diii.2017.05.004.

Deistung, A., Schweser, F., Wiestler, B., Abello, M., Roethke, M., Sahm, F., Wick, W., Nagel, A.M., Heiland, S., Schlemmer, H.-P., Bendszus, M., Reichenbach, J.R., Radbruch, A., 2013. Quantitative susceptibility mapping differentiates between blood depositions and calcifications in patients with glioblastoma. PLoS One 8, e57924. https://doi.org/10.1371/journal.pone.0057924.

Fehily, B., Fitzgerald, M., 2017. Repeated mild traumatic brain injury: potential mechanisms of damage. Cell Transplant. 26, 1131–1155. https://doi.org/10.1177/0963689717714092.

Grossman, E.J., Inglese, M., 2015. The role of thalamic damage in mild traumatic brain injury. J. Neurotrauma 167, 163–167. https://doi.org/10.1089/neu.2015.3965.

Haacke, E.M., Liu, S., Buch, S., Zheng, W., Wu, D., Ye, Y., 2015. Quantitative susceptibility mapping: current status and future directions. Magn. Reson. Imaging 33, 1–25. https://doi.org/10.1016/j.mri.2014.09.004.

Kenzie, E.S., Parks, E.L., Bigler, E.D., Lim, M.M., Chesnutt, J.C., 2017. Concussion as a multi-scale complex System , An interdisciplinary Synthesis of Current Knowledge, 8, pp. 1–17. https://doi.org/10.3389/fneur.2017.00513.

Kim, S., Pickup, S., Hsu, O., Poptani, H., 2009. Enhanced delineation of white matter structures of the fixed mouse brain using Gd-DTPA in microscopic MRI. NMR Biomed. 22, 303–309. https://doi.org/10.1002/nbm.1324.

Lehto, L.J., Sierra, A., Corum, C.A., Zhang, J., Idiyatullin, D., Pitkänen, A., Garwood, M., Gröhn, O., 2012. Detection of calcifications in vivo and ex vivo after brain injury in rat using SWIFT. NeuroImage 61, 761–772. https://doi.org/10.1016/j.neuroimage.2012.03.002.

Li, W., Long, J.A., Watts, L., Shen, Q., Liu, Y., Jiang, Z., Duong, T.Q., 2016. Spatiotemporal changes in diffusion, T_2 and susceptibility of white matter following mild traumatic brain injury. NMR Biomed. 29, 896–903. https://doi.org/10.1002/nbm.3536.

Liu, C., Li, W., Tong, K.A., Yeom, K.W., Kuzminski, S., 2015. Susceptibility-weighted imaging and quantitative susceptibility mapping in the brain. J. Magn. Reson. Imaging 42, 23–41. https://doi.org/10.1002/jmri.24768.

Liu, J., Xia, S., Hanks, R., Wiseman, N., Peng, C., Zhou, S., Haacke, E.M., Kou, Z., 2016. Susceptibility weighted imaging and mapping of micro-hemorrhages and major deep veins after traumatic brain injury. J. Neurotrauma 33, 10–21. https://doi.org/10.1089/neu.2014.3856.

Makinen, S., van Groen, T., Clarke, J., Thornell, A., Corbett, D., Hiltunen, M., Soininen, H., Jolkkonen, J., 2008. Coaccumulation of calcium and b-amyloid in the thalamus after transient middle cerebral artery occlusion in rats. J. Cereb. Blood Flow Metab. 28, 263–268. https://doi.org/10.1038/sj.jcbfm.9600529.

McIntosh, T.K., Vink, R., Noble, L., Yamakami, I., Fernyak, S., Soarest, H., Faden, a I., 1989. Traumatic brain injury in the rat: characterization of a lateral fluid-percussion model. Neuroscience 28, 233–244. https://doi.org/10.1016/0306-4522(89)90247-9.

Meconi, A., Wortman, R.C., Wright, D.K., Neale, K.J., Clarkson, M., Shultz, S.R., Christie, B.R., 2018. Repeated mild traumatic brain injury can cause acute neurologic impairment without overt structural damage in juvenile rats. PLoS One 13, e0197187. https://doi.org/10.1371/journal.pone.0197187.

Meguro, R., Asano, Y., Odagiri, S., Li, C., Shoumura, K., 2008. Cellular and subcellular localizations of nonheme ferric and ferrous iron in the rat brain: a light and electron microscopic study by the perfusion-Perls and -Turnbull methods. Arch. Histol. Cytol. 71, 205–222. https://doi.org/10.1679/aohc.71.205.

Onyszchuk, G., LeVine, S.M., Brooks, W.M., Berman, N.E.J., 2009. Post-acute pathological changes in the thalamus and internal capsule in aged mice following controlled cortical impact injury: a magnetic resonance imaging, iron histochemical, and glial immunohistochemical study. Neurosci. Lett. 452, 204–208. https://doi.org/10.1016/j.neulet.2009.01.049.

Osteen, C.L., Giza, C.C., Hovda, D.A., 2004. Injury-induced alterations in N-methyl-D-aspartate receptor subunit composition contribute to prolonged 45calcium accumulation following lateral fluid percussion. Neuroscience 128, 305–322. https://doi.org/10.1016/j.neuroscience.2004.06.034.

Osteen, C.L., Moore, A.H., Prins, M.L., Hovda, D.A., 2001. Age-dependency of 45calcium accumulation following lateral fluid percussion: acute and delayed patterns. J. Neurotrauma 18, 141–162. https://doi.org/10.1089/08977150150502587.

Özbay, P.S., Deistung, A., Feng, X., Nanz, D., Reichenbach, J.R., Schweser, F., 2017. A comprehensive numerical analysis of background phase correction with V-SHARP. NMR Biomed. 30, e3550. https://doi.org/10.1002/nbm.3550.

Rau, T.F., Kothiwal, A.S., Rova, A.R., Brooks, D.M., Poulsen, D.J., 2012. Treatment with low-dose methamphetamine improves behavioral and cognitive function after severe traumatic brain injury. J. Trauma Acute Care Surg. 73, 165–172. https://doi.org/10.1097/TA.0b013e318260896a.

Rau, T.F., Kothiwal, A.S., Rova, A.R., Brooks, D.M., Rhoderick, J.F., Poulsen, A.J., Hutchinson, J., Poulsen, D.J., 2014. Administration of low dose methamphetamine 12h after a severe traumatic brain injury prevents neurological dysfunction and cognitive impairment in rats. Exp. Neurol. 253, 31–40. https://doi.org/10.1016/j.expneurol.2013.12.001.

Reichenbach, J.R., Schweser, F., Serres, B., Deistung, A., 2015. Quantitative susceptibility mapping: concepts and applications. Clin. Neuroradiol. 25, 225–230. https://doi.org/10.1007/s00062-015-0432-9.

Robinson, S.D., Grabner, G., Witoszynskyj, S., Trattnig, S., 2011. Combining phase images from multi-channel RF coils using 3D phase offset maps derived from a dual-echo scan. Magn. Reson. Med. 65, 1638–1648. https://doi.org/10.1002/mrm.22753.

Schweser, F., Deistung, A., Lehr, B.W., Reichenbach, J.R., 2011. Quantitative imaging of intrinsic magnetic tissue properties using MRI signal phase: an approach to in vivo brain iron metabolism? NeuroImage 54, 2789–2807. https://doi.org/10.1016/j.neuroimage.2010.10.070.

Schweser, F., Deistung, A., Lehr, B.W., Reichenbach, J.R., 2010. Differentiation between diamagnetic and paramagnetic cerebral lesions based on magnetic susceptibility mapping. Med. Phys. 37, 5165–5178. https://doi.org/10.1118/1.3481505.

Schweser, F., Deistung, A., Reichenbach, J.R., 2016. Foundations of MRI phase imaging and processing for quantitative susceptibility mapping (QSM). Z. Med. Phys. 26, 6–34. https://doi.org/10.1016/j.zemedi.2015.10.002.

Schweser, F., Zivadinov, R., 2018. Quantitative susceptibility mapping (QSM) with an extended physical model for MRI frequency contrast in the brain: a proof-of-concept of quantitative susceptibility and residual (QUASAR) mapping. NMR Biomed. 31, e3999. https://doi.org/10.1002/nbm.3999.

Shah, R.N., Allen, J.W., 2017. Advances in mild traumatic brain injury imaging biomarkers. Curr. Radiol. Rep. 5, 13. https://doi.org/10.1007/s40134-017-0210-3.

Smith, D., Rau, T., Poulsen, A., MacWilliams, Z., Patterson, D., Kelly, W., Poulsen, D., 2018. Convulsive seizures and EEG spikes after lateral fluid-percussion injury in the rat. Epilepsy Res. 147, 87–94. https://doi.org/10.1016/j.eplepsyres.2018.09.005.

Straub, S., Laun, F.B., Emmerich, J., Jobke, B., Hauswald, H., Katayama, S., Herfarth, K., Schlemmer, H.-P., Ladd, M.E., Ziener, C.H., Bonekamp, D., Röthke, M.C., 2017. Potential of quantitative susceptibility mapping for detection of prostatic calcifications. J. Magn. Reson. Imaging 45, 889–898. https://doi.org/10.1002/jmri.25385.

Sun, H., Kate, M., Gioia, L.C., Emery, D.J., Butcher, K., Wilman, A.H., 2015. Quantitative susceptibility mapping using a superposed dipole inversion method: application to intracranial hemorrhage. Magn. Reson. Med. 791, 781–791. https://doi.org/10.1002/mrm.25919.

Tustison, N.J., Avants, B.B., Cook, P.A., Zheng, Y., Egan, A., Yushkevich, P.A., Gee, J.C., 2010. N4ITK: improved N3 bias correction. IEEE Trans. Med. Imaging 29, 1310–1320. https://doi.org/10.1109/TMI.2010.2046908.

Tustison, N.J., Cook, P.A., Klein, A., Song, G., Das, S.R., Duda, J.T., Kandel, B.M., van Strien, N., Stone, J.R., Gee, J.C., Avants, B.B., 2014. Large-scale evaluation of ANTs and FreeSurfer cortical thickness measurements. NeuroImage 99, 166–179. https://doi.org/10.1016/j.neuroimage.2014.05.044.

Wang, Y., Liu, T., 2015. Quantitative susceptibility mapping (QSM): decoding MRI data for a tissue magnetic biomarker. Magn. Reson. Med. 73, 82–101. https://doi.org/10.1002/mrm.25358.

Wu, B., Li, W., Avram, A.V., Gho, S.-M., Liu, C., 2012. Fast and tissue-optimized mapping of magnetic susceptibility and T2* with multi-echo and multi-shot spirals. NeuroImage 59, 297–305. https://doi.org/10.1016/j.neuroimage.2011.07.019.

Wu, B., Li, W., Guidon, A., Liu, C., 2011. Whole brain susceptibility mapping using compressed sensing. Magn. Reson. Med. 24, 1129–1136. https://doi.org/10.1002/mrm.23000.

Wu, X., Kirov, I.I., Gonen, O., Ge, Y., Grossman, R.I., Lui, Y.W., 2016. MR imaging applications in mild traumatic brain injury: an imaging update. Radiology 279, 693–707. https://doi.org/10.1148/radiol.16142535.

Yi, J.H., Hazell, A.S., 2005. N-acetylcysteine attenuates early induction of heme oxygenase-1 following traumatic brain injury. Brain Res. 1033, 13–19. https://doi.org/10.1016/j.brainres.2004.10.055.